



Experimental Sabatier plot for predictive design of active and stable Pt-alloy oxygen reduction reaction catalysts

Jin Huang¹, Luca Sementa², Zeyan Liu □¹, Giovanni Barcaro², Miao Feng¹³, Ershuai Liu⁴, Li Jiao □⁴, Mingjie Xu⁵,6, Denis Leshchev⁻, Sung-Joon Lee □¹, Mufan Li³, Chengzhang Wan³, Enbo Zhu¹, Yang Liu¹, Bosi Peng³, Xiangfeng Duan □⁵,9, William A. Goddard III □¹ ⋈, Alessandro Fortunelli □² ⋈, Qingying Jia □⁴ ⋈ and Yu Huang □¹,9 ⋈

A critical technological roadblock to the widespread adoption of proton-exchange membrane fuel cells is the development of highly active and durable platinum-based catalysts for accelerating the sluggish oxygen reduction reaction, which has largely relied on anecdotal discoveries so far. While the oxygen binding energy ΔE_0 has been frequently used as a theoretical descriptor for predicting the activity, there is no known descriptor for predicting durability. Here we developed a binary experimental descriptor that captures both the strain and Pt transition metal coupling contributions through X-ray absorption spectroscopy and directly correlated the binary experimental descriptor with the calculated ΔE_0 of the catalyst surface. This leads to an experimentally validated Sabatier plot to predict both the catalytic activity and stability for a wide range of Pt-alloy oxygen reduction reaction catalysts. Based on the binary experimental descriptor, we further designed an oxygen reduction reaction catalyst wherein high activity and stability are simultaneously achieved.

latinum alloys are the most frequently adopted electrocatalysts for accelerating the sluggish oxygen reduction reaction (ORR) at the cathode of proton-exchange membrane fuel cells (PEMFCs)^{1,2}. However, the high cost of Pt limits the practical widespread adoption of PEMFCs3-5. This has motivated intensive studies on Pt-based ORR catalysts, aiming to provide a major leap in activity and stability with reduced usage of Pt. The ORR activity is believed to scale with the core-level binding energy of oxygen to the catalyst, $\Delta E_{\rm O}$, as proposed by Nørskov et al.², which can be predicted through quantum mechanics calculations. General analysis based on the Sabatier principle indicates that a catalyst surface that binds oxygen about 0.2 eV more weakly than Pt(111) does yield the best intrinsic activity^{2,6,7}. A generally effective approach to improve ORR activity is through alloying Pt with transition metals, M (M = Pd,Fe, Co, Ni and so on)8-10, which introduces the strain effect and/or ligand effect that modulate the ΔE_0 . It has been proposed that the strain effect leads to a downshift of the Pt d-band centre relative to the Fermi level, while the ligand effect modifies the electronic structure of the near-surface Pt, both of which can weaken the ΔE_0 to improve the ORR activity¹¹⁻¹⁴.

While the quantum-mechanics-derived $\Delta E_{\rm O}$ has been widely acknowledged as a useful descriptor, its experimental analogue has met very limited success, which severely limits the efficient development of high-performing Pt-based nanocatalysts. For example, strain in Pt alloys has been routinely adopted as a plausible experimental

descriptor for ORR activity $^{14-16}$. However, strain alone is insufficient to predict the ORR activity of Pt-alloy nanocatalysts 17,18 . Meanwhile, the ligand effect 19 and local atomic coordination 20 , which describe the contributions from both composition and atomic coordination distribution to $\Delta E_{\rm O}$, and hence to the catalytic activities of Pt alloys, have rarely been investigated or accounted for experimentally because of their poor attainability in experiments. Moreover, the ever-evolving structure and composition of catalysts during catalysis 21,22 adds to the challenge of identifying simple experimentally tangible descriptors that can capture the key contributing factors predicted in theory 19,23,24 . These persisting issues have plagued the development of high-performing ORR catalysts and show the need for an experimentally tangible descriptor to predict both the activity and stability of these catalysts.

So far, the development of highly active and stable Pt-alloy nanocatalysts have largely relied on an ecdotal discoveries $^{25-27}$. Herein, by combining theoretical modelling and experimental observations, we developed a binary experimental descriptor (BED) based on the strain calculated from the average Pt–Pt bond length in the extended X-ray absorption fine structure (EXAFS; Supplementary Note 1) and the asymmetry factor (AF; Supplementary Note 2 and Supplementary Fig. 1) in the Pt $\rm L_3$ X-ray absorption near edge structure (XANES) spectra of Pt alloys. We showed that the BED can be used to accurately reflect the calculated oxygen binding energy $\Delta E_{\rm O}$ of the Pt-alloy catalyst surface (Supplementary Note 3), leading to

¹Department of Materials Science and Engineering, University of California, Los Angeles, CA, USA. ²CNR-ICCOM & IPCF, Consiglio Nazionale delle Ricerche, Pisa, Italy. ³College of Materials Science and Engineering, Fuzhou University, Fuzhou, P. R. China. ⁴Department of Chemistry and Chemical Biology, Northeastern University, Boston, MA, USA. ⁵Irvine Materials Research Institute, University of California, Irvine, CA, USA. ⁶Department of Materials Science, University of California, Irvine, CA, USA. ⁷National Synchrotron Light Source II, Brookhaven National Laboratory, Upton, NY, USA. ⁸Department of Chemistry and Biochemistry, University of California, Los Angeles, CA, USA. ⁹California NanoSystems Institute, University of California, Los Angeles, CA, USA. ¹⁰Materials and Process Simulation Center, California Institute of Technology, Pasadena, CA, USA. ¹⁰e-mail: wag@wag.caltech.edu; alessandro.fortunelli@cnr.it; qjia@iit.edu; yhuang@seas.ucla.edu

the establishment of an experimental Sabatier plot that can be used to comprehensively predict the activity and stability of Pt-alloy ORR catalysts. Furthermore, based on the established Sabatier plot, we demonstrated the design of a PtNiCo catalyst that simultaneously delivers a superior specific activity (SA) of $10.7 \pm 1.4 \, \text{mA cm}^{-2}$, a mass activity (MA) of $7.1 \pm 1.0 \, \text{A mg}_{\text{Pt}}^{-1}$ at $0.9 \, \text{V}$ versus the reversible hydrogen electrode (RHE) and an exceptionally high stability showing only 8% loss of electrochemically active surface area (ECSA) and 12% loss of MA after 20,000 cycles of accelerated degradation tests (ADTs), filling in the blank in the design space for ORR catalysts.

Results

Design and comparison of slow- and fast-dealloyed PtNi catalysts. To deconvolute and understand the key experimental signatures leading to the different activities and stabilities of Pt-alloy catalysts, we compare catalysts with similar morphologies and compositions to discern the nuanced performances. We hence chose the concave octahedral PtNi catalysts with a commonly observed stable final composition of ~80 at.% Pt and with a Pt-rich surface under electrochemical conditions^{21,28,29}. We designed and compared the performance between the fast-dealloyed PtNi (fd-PtNi) octahedral catalysts obtained through aggressive acid dealloying of the PtNi octahedral catalysts, and the slow-dealloyed PtNi (sd-PtNi) octahedral catalysts obtained through gradual dealloying in air-purged N,N-dimethylformamide (DMF). Both catalysts showed a similar concave octahedral morphology with similar composition after the electrochemical activation process (Fig. 1a-h). To prepare the concave PtNi catalysts, the transition-metal-rich octahedral parent Pt₄₅Ni₅₅/C (p-Pt₄₅Ni₅₅) was first synthesized using a modified one-pot synthesis method reported previously³⁰ (Methods). The transmission electron microscopy (TEM) and high-angle annular dark-field scanning TEM (HAADF-STEM) images (Fig. 1c) of the p-Pt₄₅Ni₅₅ showed an octahedral shape with an average edge length of 7.0 ± 0.8 nm (Supplementary Fig. 2a) and an average lattice spacing of 0.212 nm according to the fast Fourier transform diffraction pattern (inset of Fig. 1c) and X-ray diffraction results (Supplementary Fig. 3a). The p-Pt₄₅Ni₅₅ was then subject to either a slow-dealloying or a fast-dealloying process to obtain the sd-PtNi or the fd-PtNi catalysts, respectively. Both sd-PtNi and fd-PtNi showed a highly concave morphology (Fig. 1b,d) with a composition around Pt₈₅Ni₁₅ (Supplementary Figs. 3 and 4b).

To obtain sd-PtNi, the p-Pt₄₅Ni₅₅ catalysts were dispersed in DMF solution and heated to 120 °C under an air purge to allow slow dissolution of Ni (Methods). This slow process allowed additional time for the remaining atoms to rearrange themselves into a structure closer to equilibrium³¹, achieving stable, concave sd-PtNi catalysts. The changes in the structure and composition of octahedral sd-PtNi catalysts were traced by X-ray diffraction over the course of the slow dealloying (Supplementary Fig. 3a). It was observed that the main X-ray diffraction peaks shifted continuously towards low angles, indicating the lattice spacing relaxation due to transformation from Ni-rich alloys to Pt-rich alloys, and stabilized after three days of dealloying (Supplementary Fig. 3a). The average (111) lattice spacing in the sd-PtNi shifted to 0.223 nm from

0.212 nm (Supplementary Fig. 3c), indicating a composition change from Pt45Ni55 to Pt5Ni25 based on Vegard's law, which is consistent with the energy-dispersive X-ray (EDX) results (Pt₄₅Ni₅₅ to Pt₇₆Ni₂₄; Supplementary Fig. 3a). TEM studies also revealed that the octahedra evolved to the concave octahedra after three days of dealloying (Supplementary Figs. 2c and 3b). The resulting sd-Pt₇₆Ni₂₄ further evolved to highly concave sd-Pt₈₅Ni₁₅ after electrochemical activation, according to the EDX spectroscopy results (Fig. 1d and Supplementary Fig. 3f). The EDX mapping and line-scan profile of sd-Pt₈₅Ni₁₅ showed a Pt skin of about 0.7 nm after the activation process (Fig. 1g). The fd-Pt₈₆Ni₁₄ catalysts were obtained through a fast 0.5 M sulfuric acid leaching treatment of the p-Pt₄₅Ni₅₅ (Methods). The resulting fd-Pt₈₆Ni₁₄ showed a similar highly concave morphology and similar composition to the sd-Pt₈₅Ni₁₅ (Supplementary Fig. 3g), together with a similar Pt-skin structure after electrochemical activation (Fig. 1b,e and Supplementary Fig. 4c,d). In addition, the ECSA was determined to be $65\,m^2\,g_{Pt}^{-1}$ for sd-Pt₈₅Ni₁₅ and 67 m² g_{Pt}⁻¹ for fd-Pt₈₆Ni₁₄ based on the charge of the hydrogen underpotential deposition. Both values were comparable with that of commercial Pt/C (68 m² g_{Pt}⁻¹, 20 wt% Pt, Alfa Aesar) and higher than that of p-Pt₄₅Ni₅₅ (52 m² g_{Pt}^{-1} ; Supplementary Fig. 5a).

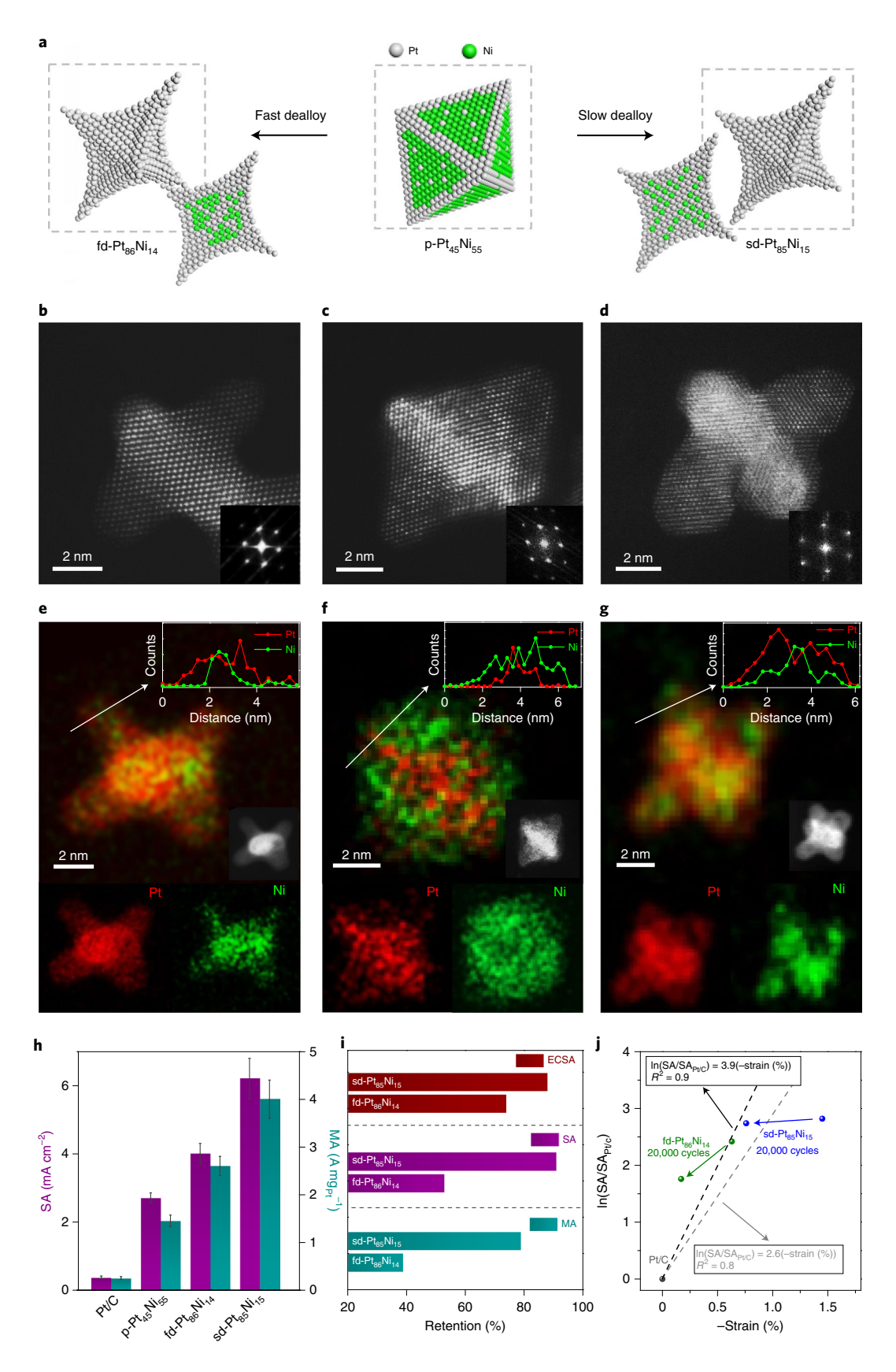
Despite the similarity in composition, highly concave morphology and Pt skin, the ORR activity and stability of the sd-Pt₈₅Ni₁₅ and fd-Pt₈₆Ni₁₄ catalysts showed considerable differences. The sd-Pt₈₅Ni₁₅ catalysts displayed a high SA of 6.2 ± 0.6 mA cm⁻² at 0.9 V versus RHE (Fig. 1h and Supplementary Fig. 5b), which was much higher than those of fd-Pt $_{86}Ni_{14}~(4.0\pm0.3~\text{mA}~\text{cm}^{-2}),\,p\text{-Pt}_{45}Ni_{55}$ $(2.7 \pm 0.2 \,\mathrm{mA \, cm^{-2}})$ and commercial Pt/C $(0.37 \pm 0.04 \,\mathrm{mA \, cm^{-2}})$. The sd-Pt₈₅Ni₁₅ showed a high MA of 4.0 ± 0.4 A mg_{Pt}⁻¹, which was about 1.5 times that of fd-Pt₈₆Ni₁₄ ($2.6 \pm 0.2 \, A \, mg_{P_t}^{-1}$), about 2.8 times that of p-Pt₄₅Ni₅₅ $(1.4\pm0.1\,\mathrm{A\,mg_{Pt}}^{-1})$ and about 16.0 times that of Pt/C $(0.25\pm0.03\,A\,mg_{Pt}^{-1}).$ Intriguingly, the durability of the sd-Pt₈₅Ni $_{15}$ and fd-Pt₈₆Ni₁₄ catalysts showed a more notable difference. After 20,000 cycles of ADT in O2-saturated HClO4, for sd-Pt85Ni15, the ECSA dropped by only 12%, the SA dropped by 9% and the MA dropped by only 21% (Fig. 1i and Supplementary Fig. 6a,b). These losses were much lower than those of the fd-Pt₈₆Ni₁₄ (47% in SA, 26% in ECSA and 61% in MA; Supplementary Fig. 7a,b) despite their similar compositions and morphologies. After ADT, it was found that the composition of sd-Pt₈₅Ni₁₅ changed to sd-Pt₉₂Ni₈ (denoted as sd-Pt₉₂Ni₈-ADT), and that that of fd-Pt₈₆Ni₁₄ changed to fd-Pt₉₅Ni₅-ADT (Supplementary Figs. 3 and 7d). Importantly, it was also found that sd-PtNi maintained the concave morphology after ADT without obvious size change (Supplementary Fig. 6c,d), whereas fd-PtNi transformed mostly into spherical nanoparticles (Supplementary Fig. 7c).

Development of BED and the Sabatier plot. To understand the structural details that render sd-Pt₈₅Ni₁₅ superior in activity and stability to fd-Pt₈₆Ni₁₄, we performed in situ X-ray absorption spectroscopy (XAS) studies. According to the in situ EXAFS spectra at the Pt L₃ edge (Supplementary Figs. 8–11 and Supplementary Table 1), the Pt–Pt bond lengths of both sd-Pt₈₅Ni₁₅ (2.71 Å) and fd-Pt₈₆Ni₁₄ (2.73 Å) are shorter compared to that of Pt/C (2.75 Å), resulting in

Fig. 1 | Design and comparison of sd-PtNi and fd-PtNi catalysts. a, Schematic illustration of the preparation of the fd-PtNi and sd-PtNi catalysts from the p-PtNi catalyst. **b-d**, Representative high-resolution atomic HAADF-STEM images for fd-Pt₈₆Ni₁₄ (**b**), p-Pt₄₅Ni₅₅ (**c**) and sd-Pt₈₅Ni₁₅ (**d**). Insets: the corresponding fast Fourier transform diffraction patterns. **e-g**, Corresponding EDX mapping and line-scan profile (following the direction of the white arrows) analysis (insets) for fd-Pt₈₆Ni₁₄ (**e**), p-Pt₄₅Ni₅₅ (**f**) and sd-Pt₈₅Ni₁₅ (**g**). **h**, Comparison of SA and MA values of p-Pt₄₅Ni₅₅, fd-Pt₈₆Ni₁₄ and sd-Pt₈₅Ni₁₅ catalysts at 0.9 V versus RHE. The error bars of all catalysts were determined from the standard deviation of ten individual measurements. **i**, Comparison of the retention of the ECSA, SA and MA of fd-Pt₈₆Ni₁₄ and sd-Pt₈₅Ni₁₅ catalysts at 0.9 V versus RHE, showing that sd-Pt₈₅Ni₁₅ has much better retention than fd-Pt₈₆Ni₁₄ in all aspects. **j**, The linear relationship between ln(SA/SA_{Pt}) and (-strain (%)) of the catalysts. The arrows indicate the value change after 20,000 cycles of ADT. The black dashed line is fitted without sd-Pt₈₅Ni₁₅ before ADT, showing a better agreement ($R^2 = 0.9$) than the grey dashed line with sd-Pt₈₅Ni₁₅ before ADT ($R^2 = 0.8$), suggesting the strain alone cannot fully account for the observed difference in SA of all the catalysts.

strain and the improved SA over Pt/C. These results confirm that the Ni-induced compressive strain benefits the ORR activity. In addition, we found that after 20,000 cycles of ADT, the Pt–Pt bond lengths of sd-Pt $_{85}$ Ni $_{15}$ and fd-Pt $_{86}$ Ni $_{14}$ relaxed to 2.73 Å and 2.75 Å,

respectively (Fig. 1j and Supplementary Table 1). This Pt–Pt bond length relaxation indicates further dealloying and structural reorganization during ADT, which leads to the decrease in SA. However, we observed that although sd-Pt₈₅Ni₁₅ experienced Pt–Pt bond



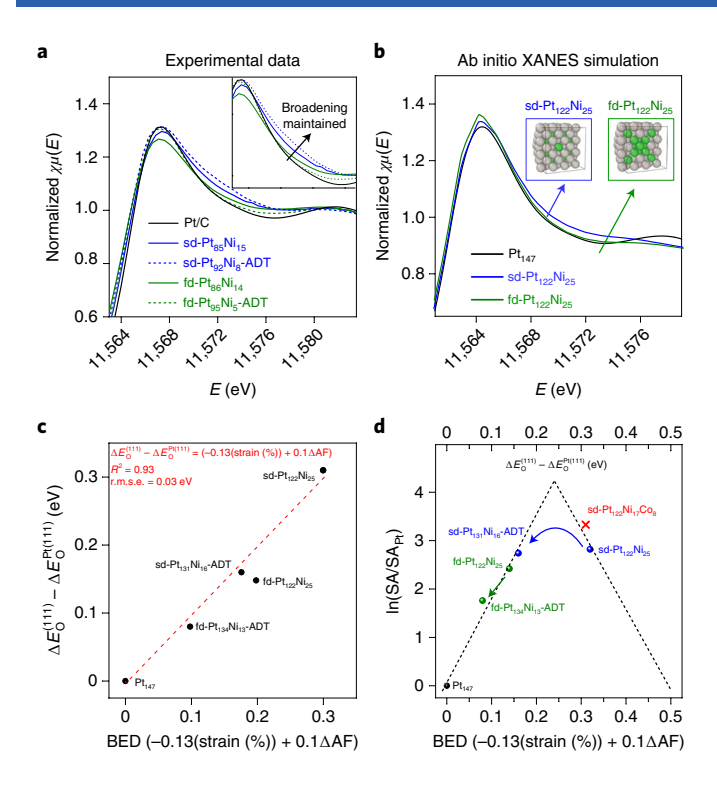


Fig. 2 | Development of the BED and the Sabatier plot. a, Experimental Pt L₃ edge in situ XANES spectra of sd-Pt₈₅Ni₁₅ (blue), sd-Pt₉₂Ni₈-ADT (blue dashed), fd-Pt₈₆Ni₁₄ (green) and fd-Pt₉₆Ni₅-ADT (green dashed) catalysts compared with Pt/C catalyst (black) collected at 0.54 V versus RHE in O₂-saturated 0.1 M HClO₄ solution. The inset panel is an enlarged region showing that the XANES broadening observed in sd-PtNi samples is maintained after ADT. $\chi\mu(E)$, the absorption coefficient. **b**, Calculated Pt L₃ edge XANES spectra for Pt₁₄₇ (black), sd-Pt₁₂₂Ni₂₅ (blue) and fd-Pt₁₂₂Ni₂₅ (green) cluster models, showing similar experimental XANES peak broadening for sd-Pt₁₂₂Ni₂₅ models. Inset: the cluster models of the sd-Pt₁₂₂Ni₂₅ and fd-Pt₁₂₂Ni₂₅ clusters. **c**, Linear regression fitting between the DFT-determined $\Delta E_{O}^{(111)} - \Delta E_{O}^{Pt(111)}$ and the BED $(-0.13(\text{strain} (\%)) + 0.1\Delta AF)$ based on the cluster models, showing good one-to-one correspondence. d, The Sabatier-like relationship between experimentally measured activity (In(SA/SA_{Pt})) of the Pt/C, sd-PtNi and fd-PtNi catalysts before and after 20,000 cycles of ADT and their corresponding simulated BED (-0.13(strain (%)) + 0.1Δ AF) based on cluster models. The top x axis is the DFT-determined difference of oxygen binding energy $\left(\Delta E_{\rm O}^{(111)} - \Delta E_{\rm O}^{\rm Pt(111)}\right)$. The red cross indicates the theoretically predicted high-performance sd-PtNiCo catalyst.

relaxation (2.71 Å to 2.73 Å) after ADT, its SA was largely maintained (from $6.2 \pm 0.6 \,\mathrm{mA \, cm^{-2}}$ to $5.6 \pm 0.3 \,\mathrm{mA \, cm^{-2}}$) compared to that of fd-Pt₈₆Ni₁₄, whereas a Pt-Pt bond relaxation from 2.73 Å to 2.75 Å has led to a more drastic change in SA from 4.0 ± 0.3 mA cm⁻² to $2.1 \pm 0.3 \,\text{mA}\,\text{cm}^{-2}$. Intriguingly, after ADT, sd-Pt₉₂Ni₈-ADT showed a considerably higher SA $(5.6 \pm 0.3 \,\mathrm{mA\,cm^{-2}})$ compared to that of the fd-Pt₈₆Ni₁₄ before ADT $(4.0 \pm 0.3 \,\mathrm{mA\,cm^{-2}})$, despite the same Pt-Pt bond length of 2.73 Å. This observation suggests that the Pt strain alone cannot fully account for the observed change in SA for sd-Pt₈₅Ni₁₅ before and after ADT. Indeed, the linear regression fittings between the logarithm of SA enhancement factor (for example, SA of Pt-alloy catalyst to the SA of Pt/C catalyst, ln(SA/SA_{Pt})) and negative strain (%) of the catalysts suggest a much better fitting without sd-Pt₈₅Ni₁₅ before ADT with a coefficient of determination of 0.9 (R^2 = 0.9) than with the sd-Pt₈₅Ni₁₅ before ADT $(R^2 = 0.8; \text{ Fig. 1j})$. This finding calls for a thorough investigation,

especially on $sd-Pt_{85}Ni_{15}$, to capture contributing factors to the catalytic activity beyond simply strain.

A further examination of the sd-Pt alloys and fd-Pt alloys before and after ADT using in situ Pt L3 XANES spectra revealed additional structural details that may contribute to the apparent difference in ORR activity and stability between the two classes of catalysts. Specifically, sd-Pt₈₅Ni₁₅ showed a considerable peak broadening in the energy range of 11,564 eV to 11,576 eV, compared to fd-Pt₈₆Ni₁₄ and commercial Pt/C (Fig. 2a), pointing to some unique atomic structural features achieved within the catalyst. XANES peak broadening was also observed for fd-Pt₈₆Ni₁₄, although to a much lesser extent (Fig. 2a). However, after 20,000 cycles of ADT, the peak broadening remained prominent in sd-Pt₉₂Ni₈-ADT, while it was nearly gone in fd-Pt₉₅Ni₅-ADT (Fig. 2a). Together with the different observed catalyst morphologies after ADT in sd-PtNi (which remained a concave octahedra; Supplementary Fig. 6c) and in fd-PtNi (which turned spherical; Supplementary Fig. 7c), these observations suggest that the peak broadening in the Pt L₃ edge XANES spectra correlates with the fine structure of Pt alloys, which may be associated with structural stability. This broadening phenomenon has been observed, although little noted, in XAS studies of intermetallic Pt alloys featuring enriched charge transfer, such as ordered intermetallic PtFe (ref. 32), PtNiCo (ref. 33) and annealed PtCu (ref. 34) and PtCo (ref. 35). In particular, the Pt L₃ edge XANES peak area has been shown to reflect multiple scatterings involving both Pt and M neighbouring atoms and the change of density of states of the 5d orbitals, where XANES peak tailing to the higher energy indicates intensified Pt-M coupling³⁶⁻³⁸. In addition, we found that annealing the p-PtNi catalysts can also lead to a broad XANES peak (Supplementary Fig. 12) together with a high Pt-Ni coordination number $(7 \pm 1; Supplementary Table 2)$. We therefore infer that the XANES peak broadening observed in sd-Pt₉₅Ni₁₅ is associated with an intimate mixing of Ni and Pt in the catalysts that facilitates the charge transfer between the Pt and Ni (refs. 36,39), denoting an intensified Pt-Ni coupling that weakens the Pt-O binding and in turn improves the intrinsic ORR activity of Pt (ref. 19). We hypothesize that the drastic broadening and the resulting tailing of the in situ Pt XANES peak towards a higher energy, observed in sd-Pt alloys, may be a characteristic feature useful for representing Pt-M coupling that encompasses a ligand effect and local atomic coordination contribution to the ORR activities in Pt-M alloys in general.

To confirm this, we constructed 147-atom cuboctahedra cluster models based on the experimental data (Supplementary Fig. 13). In addition to a pure Pt₁₄₇ cluster, we generated Pt-Ni clusters to represent fd-PtNi and sd-PtNi before and after ADT: a Pt₁₂₂Ni₂₅ cluster with Ni aggregated into the inner core and thus with the minimized number (204) of Pt-Ni nearest neighbour bonds to represent the fast-dealloying of peripheral Ni atoms in fd-Pt₈₆Ni₁₄, termed fd-Pt₁₂₂Ni₂₅; a fd-Pt₁₃₄Ni₁₃-ADT cluster with the minimized number of Pt-Ni bonds and a lower Ni content than fd-Pt₁₂₂Ni₂₅ to represent fd-Pt₉₅Ni₅-ADT; a sd-Pt₁₂₂Ni₂₅ cluster with 25 Ni and an intimate alloying of Ni and Pt in the particle core that thus maximizes the number (252) of Pt-Ni nearest neighbour bonds to represent the slow leaching together with atomic reordering of Ni into an energetically stable distribution in sd-Pt₈₅Ni₁₅; and a sd-Pt₁₃₁Ni₁₆-ADT cluster with the maximum number of Pt-Ni bonds but a lower Ni content than sd-Pt₁₂₂Ni₂₅ to represent sd-Pt₉₂Ni₈-ADT.

All clusters present a pure Pt skin. Density functional theory (DFT) geometry relaxation was performed on all structures (Methods). We then simulated XANES spectra via ab initio FEFF9 calculations⁴⁰ for the geometry-relaxed cluster models (Fig. 2b; raw data in the Supplementary Data). Notably, we observed a peak broadening in the simulated Pt L₃ XANES of the sd-Pt-alloy models with distributed Ni compared to Pt₁₄₇ (Fig. 2b), similar to the experimental XANES peaks. By contrast, no obvious peak

broadening was observed in the fd-Pt-alloy models with aggregated Ni (Fig. 2b and Supplementary Fig. 14), consistent with experimental observations (Fig. 2a). A closer look into the XANES of different sites in sd-Pt₁₂₂Ni₂₅ revealed that Pt sites featuring enriched Pt-Ni pairs showed obvious broadening, suggesting Pt-Ni coupling was in play (Supplementary Fig. 15c). The combined experimental (Fig. 2a) and computational (Fig. 2b and Supplementary Fig. 15) results so far confirmed the correlation between atomic Pt-Ni distribution in Pt alloys and Pt L₃ XANES peak broadening. Therefore, we suggest that Pt L₃ XANES peak broadening can be included in the activity descriptor for Pt-alloy nanocatalysts, together with the strain.

We use the peak AF (Methods and Supplementary Note 2 for details)41 to represent the broadening in the Pt L3 XANES peak, and further normalize the extent of the peak broadening among Pt-based catalysts to ΔAF ($\Delta AF = AF_{Pt-alloy} - AF_{Pt/C}$; Supplementary Table 3). We developed a BED descriptor (BED=A(strain (%))+B(Δ AF); Supplementary Note 3) that can be used to represent the theoretical $\Delta E_{\rm O}$, which in turn determines the ORR activity (Supplementary Fig. 16). Through optimal linear regression fitting between the DFT-predicted BED $\Delta E_{\rm O}^{(111)} - \Delta E_{\rm O}^{\rm Pt(111)}$; Supplementary Tables 3–5) and the simulated BED on all 147-atom cuboctahedra cluster models, with strain extracted from relaxed cluster structures and the ΔAF from calculated XANES spectra, we arrived at BED = -0.13(strain (%)) + 0.1Δ AF. Importantly, the optimal fitted BED showed a good linear one-to-one correspondence relationship with the calculated $\Delta E_{\rm O}^{(111)} - \Delta E_{\rm O}^{\rm Pt(111)}$, with high fidelity (R^2 =0.93, root-mean-square error (r.s.m.e.) = 0.03 eV; Fig. 2c), which is a considerably better fitting than the strain-only descriptor ($R^2 = 0.82$, root-mean-square error = 0.04 eV; Supplementary Fig. 17). Notably, the ΔAF extracted from the simulated XANES spectra also showed a linear correlation with both the Pt-M coordination number (CN_{Pt-M}) (Supplementary Fig. 18a) and the $\Delta E_{\rm O}^{\rm (111)} - \Delta E_{\rm O}^{\rm Pt(111)}$ (Supplementary Fig. 18b), confirming the direct correlation between Δ AF and CN_{Pt-M} when there is peak broadening and the impact of Δ AFon O binding on the catalyst surface. We note that Δ AF is close to zero for the fd-PtNi models regardless of bulk average CN_{Pt-Ni} (Supplementary Fig. 18a). Meanwhile our simulated XANES spectra showed vastly different broadening in Pt atoms at different locations within the same particle (Supplementary Fig. 15b) and that only sites with enriched Ni neighbours exhibit considerable broadening. We hence suggest that the AF of the XANES comprehensively reflects the Pt-M coupling, which includes both the contributions from composition (that is, average CN_{Pt-M}) and the local atomic contribution from M to Pt. There may exist a threshold value for local Ni content to demonstrate a substantial peak broadening, similar to the observation made previously with a well-defined Cu_xAu_{1-x} alloy⁴². Hence Pt-M coupling that leads to a noticeable change of the Pt d-band structure that modulates O binding on the Pt surface conveniently manifests in XANES peak broadening (Δ AF), making it a suitable experimental descriptor for $\Delta E_{\rm O}$.

We then plotted the experimental ORR activities with simulated BED, which demonstrated a clear Sabatier relationship, as one would expect for SA with the calculated $\Delta E_{\rm O}^{(111)} - \Delta E_{\rm O}^{\rm Pt(fl11)}$, suggesting that these two can be used interchangeably (Fig. 2d). Interestingly, we found that sd-Pt₁₂₂Ni₂₅ resides at the right leg (weaker Pt–O binding) of the Sabatier plot, while the fd-Pt₁₂₂Ni₂₅ resides at the left leg (stronger Pt–O binding) of the plot (Fig. 2d). This observation may be used to explain the observed better stability for sd-Pt₁₂₂Ni₂₅: upon ADT, the $\Delta E_{\rm O}^{(111)}$ of sd-PtNi decreases first, shifting the activity of sd-PtNi upward on the right slope passing the optimal peak position, and then downward along the left slope to the end position (Fig. 2d, blue points), resulting in little change in activity despite a large change in $\Delta E_{\rm O}^{(111)}$. By comparison, the fd-Pt₁₂₂Ni₂₅ starts on the left leg of the Sabatier plot, and its activity decreases mono-

tonically with the decreasing $\Delta E_{\rm O}^{(111)}$ caused by strain relaxation (Fig. 2d, green points).

The well-acknowledged instability of Pt-M ORR catalysts has been attributed to the leaching of M, which leads to the changes in both composition and structure that result in relaxed Pt-Pt strain and the decreased electronic Pt-M ligand effect^{21,43}. Hence, to retain the high activity of Pt-M catalysts, it is essential to develop a catalyst with robustness in both composition and atomic structure^{26,44,45}, since these parameters are intimately related to the activity of the catalyst. Indeed, our calculations also showed better thermodynamic stability for sd-Pt₁₂₂Ni₂₅ with a mixing energy⁴⁶ of −13.27 eV (Methods) than for fd-Pt₁₂₂Ni₂₅ (mixing energy of -12.24 eV; Supplementary Fig. 19), consistent with experimental observations of the shape retention in sd-PtNi-ADT but not in fd-PtNi-ADT. The calculation also showed that the presence of enriched subsurface Ni, particularly in the slow-dealloyed structures, largely weakens the interaction between the oxygen and the undercoordinated Pt vertex sites (Supplementary Figs. 20 and 21). The $\Delta E_{\rm O}^{\rm Vertex} - \Delta E_{\rm O}^{\rm Pt(Vertex)}$ (Supplementary Tables 3–5), defined as the difference between the $\Delta E_{\rm O}^{\rm Vertex}$ of the Pt alloy and the $\Delta E_{\rm O}^{\rm Pt(Vertex)}$ of the Pt at the vertex site, increases from $0.15 \, \text{eV}$ for fd-Pt₁₂₂Ni₂₅ alloy to $0.21 \, \text{eV}$ for sd-Pt₁₂₂Ni₂₅ alloy, suggesting weaker Pt-O binding on sd-PtNi vertex sites. The weaker Pt-O binding on these vulnerable sites protects them and increases their stability under reaction conditions^{47,48}. In addition, an even weaker Pt-O binding $\left(\Delta E_{\rm O}^{\rm Vertex} - \Delta E_{\rm O}^{\rm Pt(Vertex)}\right) = 0.28 \, \rm eV$

was found on a structurally ordered L1 $_0$ -phase L1 $_0$ -Pt₁₁₆Ni₃₁ structure (Supplementary Figs. 20 and 21), representing the more stable intermetallic phase (Supplementary Fig. 21), confirming this trend that thermodynamic stability leads to better structure stability and hence ORR stability. Together, based on this experimental Sabatier plot, we can expect that Pt-alloy catalysts with large strain and AF tend to reside on the right side of the Sabatier plot showing better stability, and those sitting closer to the top of the right slope may exhibit simultaneous high activity and high stability.

ORR catalyst design based on BED. Taking a step further, we constructed a ternary sd-Pt₁₂₂Ni₁₇Co₈ model (Methods and Supplementary Fig. 13) due to the higher chemical stability of ternary PtNiCo^{30,49,50}. For sd-Pt₁₂₂Ni₁₇Co₈, our model predicted a $\Delta E_{\rm O}^{\rm (H11)} - \Delta E_{\rm O}^{\rm Pt(H11)}$ of 0.30 eV, with a corresponding BED value of 0.30, which sits closer to the optimal position of the calculated Sabatier plot (red cross points, Fig. 2d) and demonstrates a better thermodynamic stability (calculated mixing energy of -15.11 eV; Supplementary Fig. 19). Thus, we expected that sd-Pt₁₂₂Ni₁₇Co₈ should outperform sd-Pt₁₂₂Ni₂₅ in terms of both ORR activity and stability (Fig. 2d).

We then synthesized concave PtNiCo catalyst following a similar protocol as that established for sd-Pt₈₅Ni₁₅ and obtained PtNiCo catalysts with a similar morphology and Pt composition, which were termed sd-Pt₈₄Ni₁₂Co₄ catalysts (Methods and Supplementary Figs. 22–26). As predicted, the sd-Pt₈₄Ni₁₂Co₄ showed both Pt L₃ XANES peak broadening (Fig. 3a) and compressive strain (Fig. 3b) and Supplementary Figs. 27 and 28). Similar to sd-Pt₈₅Ni₁₅, the peak broadening (AF) and the concave morphology of sd-Pt₈₄Ni₁₂Co₄ were maintained even after the 20,000 cycles of ADT (Fig. 3a,f and Supplementary Fig. 26c). As predicted, sd-Pt₈₄Ni₁₂Co₄ demonstrated superior activity to sd-Pt₈₅Ni₁₅ (Fig. 3c,d and Supplementary Fig. 25). Specifically, sd-Pt₈₄Ni₁₂Co₄ showed an impressive SA of $10.7 \pm 1.4 \,\mathrm{mA \, cm^{-2}}$ and MA of $7.1 \pm 1.0 \,\mathrm{A \, mg_{Pt}^{-1}}$ at $0.9 \,\mathrm{V}$ versus RHE, which are 28.9 times and 28.4 times, respectively, those of Pt/C (Supplementary Fig. 25b and Supplementary Table 6). Based on the experimentally determined BED and the activity of sd-Pt₈₄Ni₁₂Co₄, we found that the sd-Pt₈₄Ni₁₂Co₄ was indeed located near the top right of the Sabatier plot (Fig. 3c). Significantly, the SA of the designed sd-Pt₈₄Ni₁₂Co₄ is highly competitive among

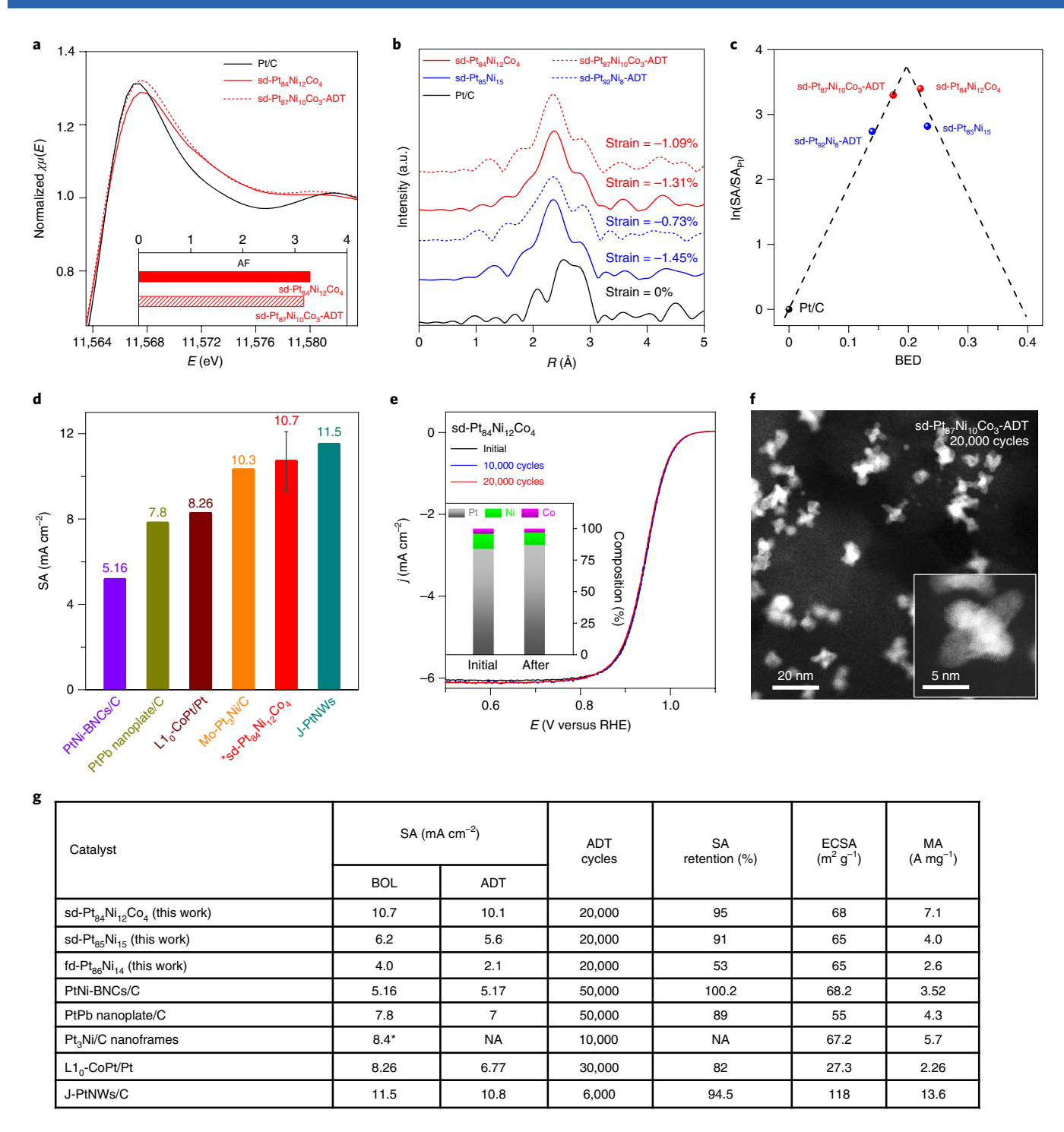


Fig. 3 | Experimentally validated sd-PtNiCo catalyst with high activity and stability. a, Pt L₃ edge in situ XANES spectra of sd-Pt₈₄Ni₁₂Co₄ (red) and sd-Pt₈₇Ni₁₀Co₃-ADT (red-dashed) compared with Pt/C catalyst (black) collected at 0.54 V versus RHE in O₂-saturated 0.1M HClO₄ solution. Inset: the AF of the concave sd-PtNiCo catalyst before and after ADT. **b**, Fourier transform of in situ EXAFS spectra of sd-Pt₈₄Ni₁₂Co₄ (red), sd-Pt₈₇Ni₁₀Co₃-ADT (red-dashed), sd-Pt₈₅Ni₁₅ (blue), sd-Pt₈₂Ni₈-ADT (blue-dashed) and Pt/C (black). In situ data were collected in an O₂-purged 0.1M HClO₄ electrolyte at 0.54 V versus RHE. *R*, radial distance. **c**, The relationship between experimentally measured activity (ln(SA/SA_{Pt})) and BED for sd-Pt₈₄Ni₁₂Co₄, sd-Pt₈₇Ni₁₀Co₃-ADT, sd-Pt₈₅Ni₁₅, sd-Pt₉₂Ni₈-ADT and Pt/C catalyst, showing a similar trend to the simulation. The dashed line is adopted from the literature⁶ with BED replacing $\Delta E_O - \Delta E_O^{Pt}$ on the *x* axis. **d**, Comparison of SA values at 0.9 V versus RHE for sd-Pt₈₄Ni₁₂Co₄ from this work (labelled with *) and other state-of-the-art ORR catalysts: PtNi bunched nanocages (PtNi-BNCs/C) (ref. ²⁶), PtPb nanoplate/C (ref. ²⁵), L1₀-CoPt/Pt (ref. ⁴⁵), Mo-Pt₃Ni/C (ref. ³¹) and J-PtNWs/C (ref. ²⁷). The error bar of the sd-Pt₈₄Ni₁₂Co₄ before ADT (black), after 10,000 cycles of ADT (blue) and after 20,000 cycles of ADT (red) between 0.6 and 1.0 V versus RHE, showing little loss in activity. Inset: the EDX-determined composition comparison before and after 20,000 cycles of ADT. *j*, current density. **f**, HAADF-STEM image of sd-Pt₈₇Ni₁₀Co₃-ADT after 20,000 cycles of ADT; inset: high-resolution STEM image. **g**, Performance of fd-Pt₈₆Ni₁₄, sd-Pt₈₈Ni₁₅ and sd-Pt₈₄Ni₁₂Co₄ catalysts compared with those in several representative works: PtNi-BNCs/C (ref. ²⁶), PtPb nanoplate/C (ref. ²⁵), Nt, not available.

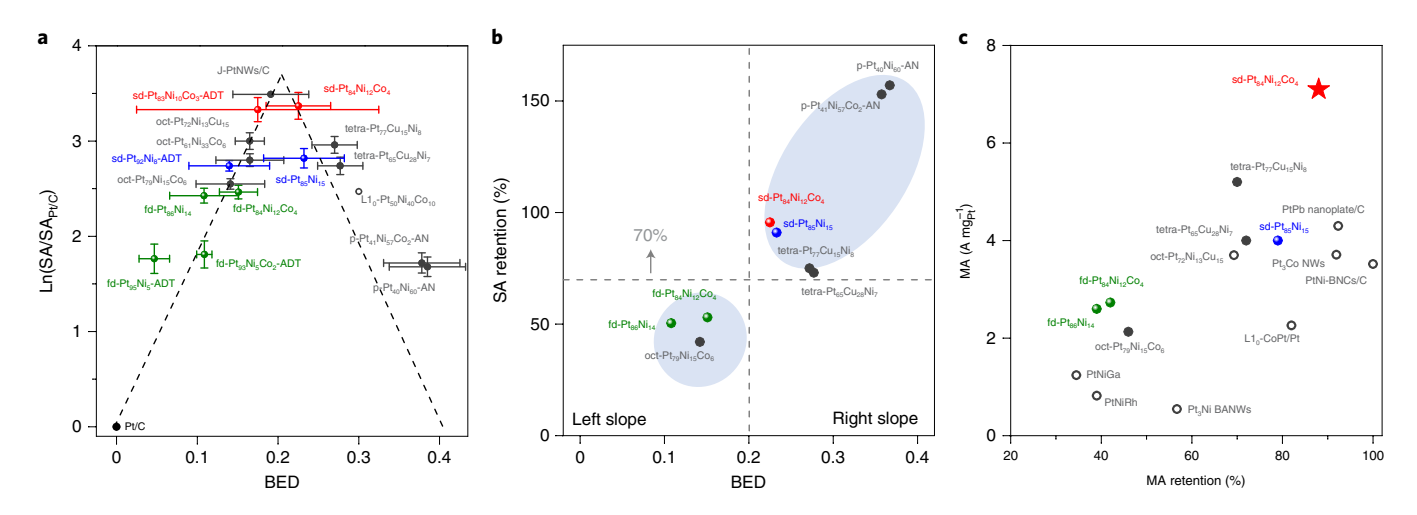


Fig. 4 | Experimentally validated Sabatier plot of Pt-alloy catalysts and stability analysis. a, Experimental Sabatier plot of Pt-alloy catalysts. The Supplementary Information describes the preparation of the tetra-PtCuNi, fd-PtNiCo, p-PtNi-AN and p-PtNiCo-AN catalysts (solid circles). Hollow circles represent catalysts reported in the literature: $L1_0$ -Pt₅₀Ni₄₀Co₁₀ (ref. 33), J-PtNWs/C (ref. 27), oct-Pt₇₂Ni₁₃Cu₁₅ (ref. 44) and oct-Pt₆₁Ni₃₃Co₆ (the composition was determined before activation)⁵⁰. The dashed line is adopted from the literature⁶ with BED replacing $\Delta E_0 - \Delta E_0^{\text{pt}}$ on the *x* axis. The error bars of BED consist of the uncertainties of strain from the EXAFS fitting and the uncertainties of Δ AF measured in ten XANES spectra. The activity error bars were determined from the standard deviation of ten individual measurements. **b**, Comparison of SA retention for left-slope catalysts and right-slope catalysts after 20,000 cycles of ADT between 0.6 V and 1.0 V versus RHE at a sweep rate of 100 mV s⁻¹ in O₂-saturated 0.1 M HClO₄. The horizontal dashed line indicates 70% SA retention. The vertical dashed line is the separation line for the left slope and the right slope. The two groups of catalysts are indicated in two shaded areas to show distinction. **c**, MA and MA retention of Pt-alloy catalysts (with at least 20,000 cycles of ADT), showing that sd-PtNiCo (labelled with a red star) possesses both high MA and high MA retention. Hollow circles represent catalysts reported in the literature: PtPb nanoplate/C (ref. 25), PtNi-BNCs/C (ref. 26), L1₀-CoPt/Pt (ref. 45), oct-Pt₇₂Ni₁₃Cu₁₅ (ref. 44), Pt₃Ni BANWs, Pt₃Ni bimetallic alloy nanowires (ref. 40), PtNiRh (ref. 65), PtNiGa (ref. 66) and Pt₃Co nanowires (Pt₃Co NWs) (ref. 67). Solid circles represent catalysts made and tested in the same research group.

state-of-the-art Pt-based catalysts, including Mo-doped Pt₃Ni (ref. ⁵¹) and state-of-the-art jagged Pt nanowires (J-PtNW/Cs²⁷; Fig. 3d,g). More importantly, the sd-Pt₈₄Ni₁₂Co₄ also showed simultaneously exceptional stability with only 8% loss of ECSA, 5% loss of SA and 12% loss of MA after the ADT (Fig. 3e, Supplementary Fig. 26b and Supplementary Table 6), all superior to the values of sd-Pt₈₅Ni₁₅, as predicted. The composition of the sd-Pt₈₄Ni₁₂Co₄ stayed essentially unchanged after 20,000 cycles of ADT (inset of Fig. 3e and Supplementary Fig. 23), and the concave morphology of sd-Pt₈₄Ni₁₂Co₄ was also largely maintained (Fig. 3f and Supplementary Fig. 26c; the percentage of concave shape is 78% after ADT in comparison to 88% before ADT). Importantly, the XANES peak broadenings weres also observed on ex situ samples (Supplementary Fig. 29), making the BED more practical to obtain experimentally and apply in catalyst performance prediction.

Our proposed BED thus fully accounts for the experimentally observed ORR activities for sd-Pt alloys and fd-Pt alloys before and after ADT (Fig. 3c), which leads to an experimental Sabatier plot to predict the Pt-alloy activity (SA) based on the experimentally measurable value -0.13(strain (%))+0.1 Δ AF. On this experimental Sabatier plot, the sd-Pt alloys started on the right slope before the ADT, and landed on the left slope after the ADT. During this process, the strain and the Pt-M coupling (the local coordination environment that contributed to the broadening of the Pt L₃ edge in situ XANES spectra) might work synergistically to preserve the activity of the sd-Pt alloys. Hence, Pt alloys with such XANES peak broadening feature may still maintain a $\Delta E_{c}^{(111)}$ closer to the optimal value despite the lattice relaxation during the long-term electrocatalytic reactions, exhibiting robust stability. This observation suggests that Pt-alloy catalysts whose BED lies on the right slope of the Sabatier plot, usually those with large strain and/or Δ AF, may exhibit better stability than those with a BED on the left.

Discussion

To examine the universality of the descriptor, we examined various Pt-alloy catalysts (Supplementary Information for the synthesis details) with different morphologies, structures and compositions (Supplementary Tables 2 and 3 and Supplementary Figs. 30-32). With the experimentally measured activity $\ln(SA_{Pt\text{-alloy}}/SA_{Pt/C})$ as the *y* axis, and the BED in place of $\Delta E_{O}^{(111)} - \Delta E_{O}^{Pt(111)}$ on the *x* axis, we found that all examined catalysts fall nicely into the predicted experimental Sabatier relation (Fig. 4a). As shown in the plot, the Pt-based catalysts without XANES broadening (or a negligible Δ AF) all reside at the left side of the Sabatier plot, including the previously reported J-PtNWs/C, which sit near the top left of the plot (Fig. 4a). The intermetallic Pt alloy (extracted from the literature³³), the tetrahedral PtCuNi alloys (tetra-PtCuNi) and the annealed p-Pt alloy (p-Pt-alloy-AN) all reside on the right slope of the Sabatier plot, showing considerable broadening in their Pt L₃ XANES peaks and large strain. We expect that this BED can predict ORR activities for virtually all Pt-based catalysts without prior knowledge of the composition, morphology or structure. We also expect that this BED can be used to qualitatively predict the stability of Pt-alloy catalysts, based on which side of the slope they reside on. We hypothesize that similar to sd-PtNi and sd-PtNiCo, Pt alloys located on the right side of the experimental Sabatier plot may demonstrate higher stability than those on the left. We further investigated the stability (20,000 cycles of ADT) of the catalysts on the left and the right slope (Fig. 4b). As expected, the catalysts located on the right slope of the experimental Sabatier plot all showed an excellent SA retention above 70%, including sd-Pt alloys, tetra-PtCuNi and the annealed p-PtNi-AN and p-PtNiCo-AN. Interestingly, the p-PtNi-AN and p-PtNiCo-AN located at the lower side of the right slope showed an even higher SA after ADT than that at which they started (retention about 150%; Supplementary Fig. 31i-l), indicating that ADT process led to a decreased BED (and hence $\Delta E_{\rm O} - \Delta E_{\rm O}^{\rm Pt}$) and

shifted the SA up the right side of the Sabatier plot. By contrast, those Pt-alloy catalysts located at the left slope usually showed a lower SA retention around 50%, consistent with the expectation. Therefore, the BED can capture the contributions from both the strain effect and Pt-M coupling effect to reflect the calculated oxygen binding energy $(\Delta E_{\rm O} - \Delta E_{\rm O}^{\rm Pt})$ in Pt-alloy catalysts, and can be used to predict both the activity and stability of ORR catalysts. We expect that the Pt alloys located near the top of the right slope may present the most desirable ORR catalysts, possessing both high SA and high stability, such as the sd-PtNiCo designed in this study. In addition to a large and stable ECSA, the sd-PtNiCo showed a simultaneous high MA of $7.1 \pm 1.0 \,\mathrm{Amg_{Pt}}^{-1}$ and MA retention of 88%, showing the optimal combination of activity and stability among the state-of-the-art ORR catalysts (Fig. 4c). Importantly, the excellent ORR performance of sd-PtNiCo has also been realized in a membrane electrode assembly (MEA), suggesting its applicability in a practical fuel cell. In MEA, the sd-PtNiCo exhibited a high MA of $0.67 \pm 0.03\,\mathrm{A\,mg_{Pt}^{-1}}$ and considerable MA retention of 64% after 30,000 square wave cycles of accelerated stress tests at a cathode loading of 0.083 mg_{Pt} cm⁻² (Methods and Supplementary Figs. 33 and 34).

In summary, by comparing the structure-function relationship of concave octahedral sd-PtNi and fd-PtNi catalysts, we found that compressive strain and Pt-Ni coupling can be cumulatively captured with a BED descriptor (BED = -0.13(strain (%)) + 0.1Δ AF) that can be used in a way similar to the DFT-calculated ΔE_0 to predict the ORR activity of Pt-alloy catalysts. The BED works generally well to describe the experimentally observed ORR activities for Pt-alloy catalysts, confirming a Sabatier relation that can be used to predict both the activity and the stability of the Pt-based ORR catalysts. Based on this BED, we designed a sd-Pts4Ni12Co4 catalyst residing near the top of the right leg of the Sabatier plot, which exhibited a simultaneously high SA of 10.7 ± 1.4 mA cm⁻² and excellent stability, showing only 8% loss of ECSA, 5% loss of SA and 12% loss of MA after 20,000 cycles of ADT. The high activity and stability of the sd-PtNiCo catalysts have also been validated in a MEA full cell, with both MA and stability surpassing targets set by the US Department of Energy.

Methods

Chemicals. Platinum(II) acetylacetonate (Pt(acac)2, 97%), nickel(II) acetylacetonate (Ni(acac), 95%), cobalt(II) acetylacetonate (Co(acac), 97%), copper(II) acetylacetonate (Cu(acac)2, 97%), perchloric acid (HClO4, 70%, impurity level in the low parts per 1012 (ppt) grade), glucose, benzoic acid (C₆H₅COOH, \geq 99.5%), oleylamine (OAm; CH₃(CH₂)₇CH=CH(CH₂)₇CH₂NH₂, >70%), 1-octadecene (ODE; CH₂=CH(CH₂)₁₅CH₃; technical grade, >90%) and 5 wt% Nafion were all purchased from Sigma-Aldrich. Commercial Pt/C catalyst (20 wt% Pt, particle size 2 to 5 nm), Pt/C catalyst (10%) and Pt/C catalyst (40%) were purchased from Alfa Aesar. DMF (≥99.8%), ethanol (200 proof) and cyclohexane (C₆H₁₂; analytical reagent, >99.5%) were obtained from EMD Millipore and Decon. Acetone (≥99.5%) and isopropanol (≥99.5%) were purchased from Fisher Scientific. All reagents were used as received without further purification. Carbon black (Vulcan XC-72) was received from Carbot Corporation and annealed in 280 °C air before use. Deionized water (18 MΩ cm⁻¹) was obtained from an ultra-pure purification system (Milli-Q Advantage A10). The Nafion HP membrane and gas diffusion electrode were purchased from Fuel Cell store.

Preparation of p-Pt-alloy catalysts. In a typical synthesis of p-Pt₄₅Ni₅₅ catalysts, $10\,mg$ Pt(acac)₂, $20\,mg$ Ni(acac)₂ and $250\,mg$ benzoic acid were added to $10\,ml$ of a solution of carbon black suspended in DMF (total $30\,mg$ carbon black) in a $35\,ml$ glass vial. The mixture was ultrasonicated for $10\,min$, heated to $160\,^{\circ}C$ and kept at that temperature for $12\,h$ with stirring in an oil bath. After reaction, the vial was cooled to room temperature; the p-Pt₄₅Ni₅₅ catalyst was obtained by centrifugation, washed with an isopropanol/acetone mixture several times and dried in a vacuum dryer. The synthesis of p-Pt₄₁Ni₅₄Co₅ octahedra was similar to the above protocol except an additional $5\,mg$ Co(acac)₂ was added.

Preparation of sd-Pt-alloy catalysts. First, 200 mg p-Pt-alloy catalyst was dissolved with 150 ml DMF in a 250 ml three-neck flask and sonicated for 20 min. Then, the three-neck flask with stirring was put into the oil bath and heated to 120 °C. The solution was purged with air and refilled with DMF to maintain a

constant level of solution. The sample was collected at different times, centrifuged and washed with an isopropanol/acetone mixture. The resulting sd-Pt alloy was further dried in a vacuum dryer.

Preparation of fd-Pt-alloy catalysts. The preparation of fd-Pt-alloy catalysts was achieved by annealing p-Pt-alloy catalysts in air at 120 °C for 2 h to mimic the dealloying condition of sd-Pt-alloy catalysts. Then, the annealed catalysts were dealloyed in 0.5 M $\rm H_2SO_4$ at 80 °C for 2 h. The sample was collected by centrifugation and then washed with deionized water until the pH was neutral. The resulting fd-Pt-alloy catalysts were further dried in a vacuum dryer.

Preparation of tetrahedra PtCuNi catalysts. The synthesis of tetrahedra PtCuNi (tetra-PtCuNi) catalysts is based on a previous report 52 . In a typical synthesis of tetra-Pt $_{77}$ Cu $_{15}$ Ni $_8$ catalysts, Pt(acac) $_2$ (20 mg), Cu(acac) $_2$ (6 mg), Ni(acac) $_2$ (6 mg), glucose (135 mg), OAm (3 ml) and ODE (2 ml) were added to a 35 ml vial. The mixture was ultrasonicated for 1 hour, purged with carbon monoxide (CO) for 5 min and heated to 170 °C in 0.5 h and kept for 12 h in an oil bath with stirring. After cooling to room temperature, the colloidal products were collected and washed with a cyclohexane/ethanol mixture (v/v=1:5) two times. The synthesis of tetra-Pt $_{65}$ Cu $_{28}$ Ni $_7$ was similar to the above protocol except an additional 12 mg Ni(acac) $_2$ was used. The as-prepared tetra-PtCuNi catalysts were dispersed in a 20 ml cyclohexane/ethanol mixture (v/v=1:1) containing carbon black (20 mg) and sonicated for 2 h. The resulting catalysts were collected by centrifugation and washed with a cyclohexane/ethanol mixture. After drying, the catalysts were annealed at 130 °C for 6 h in Ar (100 sccm) in a home-built tube furnace. The composition was determined by EDX after the catalysts were activated.

Preparation of p-Pt-alloy-AN catalysts. The p-PtNi-AN and p-PtNiCo-AN catalysts were prepared by annealing the p-PtNi and p-PtNiCo catalysts in a home-made furnace at $700\,^{\circ}$ C for 2h with a mixture of gas flow (Ar/H₂= $300\,$ sccm: $3\,$ sccm).

Preparation of octahedral $Pt_{79}Ni_{15}Co_6$ catalysts. The $Pt_{79}Ni_{15}Co_6$ (oct- $Pt_{79}Ni_{15}Co_6$) catalysts were synthesized with a method similar to that previously reported catalysts were synthesized with a method similar to that previously reported catalysts were added to 10 ml of a solution of carbon black suspended in DMF (total 30 mg carbon black) in a 35 ml glass vial. The vial was then capped and ultrasonically processed for 20 min, followed by heating with magnetic stirring in an oil bath at 160 °C for 12 h. After reaction, the vial was cooled to room temperature. The oct- $Pt_{79}Ni_{15}Co_6$ catalyst was obtained by centrifugation and washed with an isopropanol/acetone mixture several times. The resulting catalyst was dried in a vacuum dryer.

Structure and composition characterization. Powder X-ray diffraction patterns were collected on a Panalytical X'Pert Pro X-ray powder diffractometer with Cu $K\alpha$ radiation. Low-magnification TEM images were taken on a FEI T12 transmission electron microscope operated at 120 kV. High-resolution TEM images, EDX line-scan files and HAADF-STEM images were taken on a JEM-ARM300F Grand ARM operated at 300 kV. TEM samples were prepared by dropping an ethanol dispersion of catalysts onto carbon-coated aluminium TEM grids. The Pt loading of catalysts was determined by inductively coupled plasma atomic emission spectroscopy. The Pt loading was determined before electrochemical measurement. The Pt loading is about 10.6 wt% for p-Pt alloys and about 9.5 wt% for sd-Pt alloy and fd-Pt alloys.

Electrochemical measurement. A three-electrode cell system was used to conduct all electrochemical tests. The working electrode was a glassy carbon rotating disc electrode with a 0.196 cm² glassy carbon geometry area, from Pine Instruments. The counter and reference electrodes were Pt wire and Ag/AgCl (1 M Cl⁻), respectively. For activity measurement, Pt loadings were 7.85 μg cm⁻², 7.65 μg cm⁻², $5.65\,\mu g\,cm^{-2}$ and $5.55\,\mu g\,cm^{-2}$ for $p\text{-Pt}_{45}Ni_{55},\,p\text{-Pt}_{41}Ni_{54}Co_5,\,sd\text{-Pt}_{85}Ni_{15}$ and sd-Pt₈₄Ni₁₂Co₄, respectively. The Pt loadings of fd-Pt alloy and Pt/C catalysts were about 7.5 $\mu g\,cm^{-2}$ and 10 $\mu g\,cm^{-2}$, respectively. Cyclic voltammetry (CV) activations were performed in N₂-saturated 0.1 M HClO₄ electrolyte with a potential scan rate of 100 mV s⁻¹ from 0.05 to 1.1 V versus RHE, until cyclic voltammetry curves stabilized. The ECSA was determined by integrating the hydrogen underpotential deposition area (H_{upd}) on the CV curve by taking a value of 210 μ C cm⁻² for the adsorption of one monolayer of hydrogen. The ORR was tested in an O2-saturated 0.1 M HClO₄ electrolyte with a potential scan rate of 20 mV s⁻¹. The measurement temperature was set at 25 °C using a water bath five-neck flask. The current density of the ORR polarization curves was resistance corrected (iR) and background corrected. The ADT were performed at room temperature in O2-saturated 0.1 M HClO₄ solutions by applying CV sweeps between 0.6 and 1.0 V versus RHE at a sweep rate of 100 mV s⁻¹.

Membrane electrode assembly preparation and single fuel cell test. The single fuel cell performance of the catalysts as the cathode was tested with an 850e Fuel Cell Test System (Scribner). The membrane electrode assemblies with an active area of 5.0 cm² were fabricated using the catalyst-coated membrane method. The anode loading was set to be 0.025 mg_{Pt} cm⁻² (10% Pt/C, Alfa Aesar). Catalysts

were incorporated into membrane electrode assemblies by direct spraying of a water/2-propanol-based ink onto a Nafion HP membrane with a loading of 0.083 mg $_{\rm Pt}$ cm $^{-2}$. The mass activity was measured via measuring the current at 0.9 $V_{\rm IR-free}$ ($V_{\rm IR-free}$ resistance-corrected voltage) under 150 kPa $_{\rm abs}$ (abs, absolute pressure) $\rm H_2/O_2$ (80 °C, 100% relative humidity, $\rm H_2/O_2$ = 835:2,000 sccm) with $\rm H_2$ crossover correction. The potential cycling accelerated stress tests were conducted using the square wave method from 0.6 V to 0.95 V with 3 s hold time at each potential (150 kPa $_{\rm abs}$ $\rm H_2/N_2$, 80 °C, 100% relative humidity, $\rm H_2/N_2$ = 100:100 sccm). The $\rm H_2/air$ test was conducted under 250 kPa $_{\rm abs}$ $\rm H_2/air$ (94 °C, 100% relative humidity, $\rm H_2/air$ = 1.5:1.8 stoichiometry, 126:358 sccm).

XAS data collection and analysis. The electrode inks for the XAS electrodes were similar to the rotating disc electrode. The ink was drop-cast onto a carbon paper with a total catalyst loading of about 8 mg cm⁻². For convenience, examined catalysts were activated on the three-electrode system prior to XAS measurements. The ADT samples were cycled following the same protocol as on the rotating disc electrode. The XAS experiments were conducted at room temperature in a previously described in situ spectro-electrochemical half cell in which a continuously O₂-purged 0.1 M HClO₄ aqueous solution was circulated⁵³, at beamlines ISS 6-BM and 8-ID at the National Synchrotron Light Source II (Brookhaven National Laboratory, NY). Before transfer into the cell, the electrodes were conditioned in 0.1 M HClO₄ under vacuum for 40 min to remove surface oxides and contaminants. Potentiostatic control was maintained with an Autolab PGSTAT30 potentiostat (Metrohm USA, formerly Brinkman Instruments). Full-range Pt L₃ edge, Ni K edge and/or Co K edge spectra were taken at various static potentials along the anodic sweep of the CV. Data were collected on the same electrode in transmission mode at the Pt L3 edge, and fluorescence mode at the Ni and/or Co K edge, with a Pt/Co/Ni reference foil positioned between the ionization chambers I2 and I3 as a reference. The voltage cycling limits were 0.05 to 1.00 V versus RHE. Data collection was performed at the chosen potentials held during anodic sweeps. The electrode was fully cycled following each potential hold to clean the electrode surfaces after each potential hold. Typical experimental procedures were utilized with details provided in our previous work⁴³. The data were processed and fitted using the IFEFFIT-based Athena⁵⁴ and Artemis⁵⁵ programmes. Scans were calibrated, aligned and normalized with background removed using the IFEFFIT suite⁵⁶ The Fourier transform magnitudes ($\chi(R)$) were modelled using single scattering paths calculated by FEFF6 (ref. 57).

By comparison, traditional first-shell EXAFS analysis was performed on studied samples with similar parameter settings. The fits were conducted at the Pt L₃ and Ni K edges concurrently for beginning of life samples, but for ADT samples the fits were conducted only at the Pt L₃ edge since the Ni is in a mixed form of metallic and oxidative phases and cannot be fitted. The fitting results are listed in Supplementary Table 1. A Pt₃Ni₁ face-centered cubic cluster model was used for EXAFS fitting. The first-shell Pt–Pt and Pt–Ni paths and Ni–Pt and Ni–Ni paths were included for fitting at the Pt L₃ edge and Ni K edge, respectively. Basic constraints $R_{\text{Pt-Ni}} = R_{\text{Ni-Pt}}$ and $\sigma^2_{\text{Pt-Ni}} = \sigma^2_{\text{Ni-Pt}}$ were introduced during the fitting. Here $R_{\text{Pt-Ni}}(R_{\text{Ni-Pt}})$ is the bond distance for Pt–Ni (Ni–Pt) scattering, and $\sigma^2_{\text{Pt-Ni}}(\sigma^2_{\text{Ni-Pt}})$ is the Debye–Waller factor of the bond lengths given by the fitting. Owing to the low content of Co in the sd-PtNiCo catalyst and the fact that Ni and Co cannot be distinguished by XAS as scattering neighbours, these restrictions were applied for the sd-PtNiCo as well.

Computational studies. The XANES spectra were simulated by employing the FEFF9 code 57 , which calculates the self-consistent multiple scattering from atomic targets whose scattering potential is obtained by overlapping free atom densities in the muffin tin approximation 58 . We calculated the Pt $\rm L_3$ edge structure for 147-atom cuboctahedral cluster models as described below and depicted in Supplementary Fig. 13, and we reported them, usually averaged over all atoms. Simulated XANES spectra of individual Pt atoms are also reported in the main text.

Quantum mechanical DFT calculations were performed on PtNi clusters of up to 147 atoms in size. For each cluster model, full local geometry relaxation was performed starting from the geometry of Pt_{147} . We used the Quantum Espressos suite of programs, the Perdew–Burke–Ernzerhofe exchange–correlation functional and ultra-soft pseudopotentials local geometry optimizations were performed spin unrestricted and employed the following numerical parameters: wavefunction and charge-density cut-offs equal to 40 and 400 Ry, respectively, a simple cubic cell with side length of 20 a.u., a Gaussian smearing of the one-electron energy levels of 0.001 a.u., a convergence threshold for self-consistency equal to $0.5 \times 10^{-6}\,\mathrm{a.u.}$ and a reciprocal space sampled at the gamma point only. Geometries were considered to be converged when the forces on each atom became smaller than 0.001 a.u.

The models investigated in this work are based on a 147-atom cluster of cuboctahedral symmetry (Supplementary Fig. 13). Atoms in this cluster can be distinguished into nine symmetry-equivalent groups or orbits¹⁶: one atom at the centre (orbit (i)), a first shell of 12 first neighbours (orbit (ii)), six atoms on subsurface (100) facets (orbit (iii)), 24 atoms on subsurface (111) facets (orbit (iv)), 12 atoms on subsurface vertexes (orbit (v)), eight atoms on (111) surface facets (orbit (vi)), 24 atoms on (100) surface facets (orbit (vii)), 48 atoms on surface edges

(orbit (viii)) and 12 atoms on surface vertexes (orbit (ix)). By distributing different numbers of Ni (or Co) atoms, replacing Pt atoms, in this cuboctahedral structural framework, after geometry relaxation we obtain clusters with varying compositions and compositional orders (Supplementary Fig. 13) that model the stoichiometry and structural features of the different systems produced experimentally. The Cartesian coordinates of these models are reported at the end of the Supplementary Data file. We thus considered one pure Pt model, Pt₁₄₇, and two Pt₁₂₂Ni₂₅, one $Pt_{131}Ni_{16}$, one $Pt_{134}Ni_{13}$, one $Pt_{116}Ni_{31}$ and one $Pt_{122}Ni_{17}Co_8$ models. In detail, in the mixed sd-Pt₁₂₂Ni₂₅, the 25 Ni atoms were distributed in orbits (i) and (iv), therefore maximizing the number of Pt-Ni bonds. In the segregated fd-Pt₁₂₂Ni₂₅, the same number of 25 Ni atoms were distributed in orbits (i), (ii) and (v). The sd-Pt₁₂₂Ni₂₅ thus mimics an ordered arrangement of Ni in the cluster, as obtained via a slow leaching together with atomic reordering of Ni into an energetically stable distribution, whereas fd-Pt₁₂₂Ni₂₅ mimics a more aggregated arrangement of Ni atoms in the structural framework, as obtained via a fast leaching of the most peripheral Ni atoms.

By electrochemical ADT, further Ni is leached out of the clusters; our model uses two more clusters: (1) in the mixed sd-Pt₁₃₁Ni₁₆-ADT, we started from sd-Pt₁₂₂Ni₂₅, depleted orbit (i) of Ni and replaced one Ni atom with one Pt from each (111) subfacet site (that is, orbit (iv)) to obtain a still reasonably symmetric, strongly mixed and stable Ni distribution but a lower Ni content; and (2) in the segregated fd-Pt134Ni13-ADT, we started from fd-Pt122Ni25 and depleted orbit (v) of Ni to obtain a strongly segregated and dealloyed cluster. Finally, a sd-Pt₁₂₂Ni₁₇Co₈ model was built by replacing one Ni atom of sd-Pt122Ni25 with one Co from each subsurface (111) facet of orbit (iv) to obtain a cluster with the same number of dopant atoms as sd-Pt $_{122}$ Ni $_{25}$ and fd-Pt $_{122}$ Ni $_{25}$ for direct comparison with the experimental particles; this cluster mimics a slow-dealloying process of a PtNiCo particle. For completeness, we also considered a L1₀-Pt₁₁₆Ni₃₁ cluster, in which the Ni atoms are distributed in the core according to a L10-bulk-like chemical ordering, that is, with Pt and Ni alternating in (100) layers. Note that the stoichiometry of our cluster models tries to resemble the experimental ones, given the constraints due to the smallness of our clusters. The geometry of these cluster models was fully relaxed at the Perdew-Burke-Ernzerhof level of DFT, and then used to simulate XANES spectra with the FEFF9 code.

Finally, we calculated oxygen adsorption energies on various sites of the so-derived cluster models (Supplementary Figs. 16 and 19) after full geometry relaxation as $\Delta E_{\rm O} = E(M_{\rm 147}-{\rm O}) - E(M_{\rm 147}) - E({\rm O}_{\rm gas-phase})$, where all energies are taken at the corresponding equilibrium geometries. We considered the interaction of O adatoms both on the face-centered cubic (111) adsorption sites (as models of the ORR mechanism, to be related to ORR activity) and on vertex sites (as models of particle oxidation/degradation, to be related to the stability of the clusters (as models of the total considered the case of multiple possible adsorption sites inequivalent by symmetry, we took the average adsorption energy to build the plots in the main text and Supplementary Fig. 16.

In detail, the O binding energy, $\Delta E_{\rm O}$, is calculated as

$$\Delta E_{\rm O} = E(M_{147} - O) - E(M_{147}) - E(O_{\rm gas-phase}),$$
 (1)

where M_{147} is the 147-atom Pt or Pt-alloy cluster model, $E(M_{147}-O)$ is the total energy of a cluster with O binding on a 147-atom Pt or Pt-alloy cluster, $E(M_{147})$ is the total energy of the 147-atom Pt or Pt-alloy cluster without adsorbates and $E(O_{\rm gas-phase})$ is the total energy of an oxygen atom in the gas phase.

In the main text, $\Delta E_{\rm O}^{\rm Pt-anor}$ is the otal energy of an oxygen atom in the gas phase. In the main text, $\Delta E_{\rm O}^{\rm (11)}$ represents the average $\Delta E_{\rm O}$ on the (111) sites of the 147-atom Pt-alloy cluster, $\Delta E_{\rm O}^{\rm Pt(111)}$ $\Delta E_{\rm O}^{\rm Pt(111)}$ or represents the average $\Delta E_{\rm O}$ on the (111) sites of the Pt₁₄₇ cluster, $\Delta E_{\rm O}^{\rm Vertex}$ represents the $\Delta E_{\rm O}$ on the vertex site of the 147-atom Pt-alloy cluster and $\Delta E_{\rm O}^{\rm Pt(Vertex)}$ represents the $\Delta E_{\rm O}$ on the vertex site of the Pt₁₄₇ cluster.

Note that, in analogy with previous literature⁴⁸, we used the oxygen adsorption on the vertex site and the mixing energy (that is, the formation energy; Supplementary Fig. 19) of the clusters as descriptors of their stability (that is, their smaller tendency to Pt oxide formation). Although the topic of aqueous dissolution is important and the focus of current active research, and more advanced approaches have recently been proposed⁶², our assumption is reasonable considering, for example, that experimentally, a surface metal oxide on edges and vertexes of Pt nanoparticles has been proven to increase the catalyst stability by protecting undercoordinated and more strongly oxygen-interacting Pt sites such as vertex ones⁴⁷.

Note that we use an isolated oxygen atom in the gas phase as a reference. Another reference state for reporting oxygen adsorption, commonly used in previous literature, is the O_2 molecule in the gas phase. To convert the two, it is sufficient to add a positive term of $\frac{1}{2}E(O_{2,gas-phase}) - E(O_{gas-phase}) = 2.8 \, eV$ to our O adsorption number.

The mixing energy⁴⁶ of an A-B alloy is defined as

$$\Delta (N_{A}, N_{B}) = E_{\text{alloy}} (N_{A}, N_{B}) - N_{A} E_{A} (N) / N - N_{B} E_{B} (N) / N$$
 (2)

where $E_{\rm alloy}(N_A, N_B)$ is the energy of a nanoalloy cluster composed of N_A atoms of species A and N_B atoms of species B; $N = N_A + N_B$ is the total number of atoms in the cluster; $E_A(N)$ is the energy of a pure-A cluster of N atoms; and $E_B(N)$ is the energy of a pure-B cluster of N atoms.

Data availability

The atomic coordinates of the DFT calculation data and simulated XANES data are available in the Supplementary Data. The data that support the findings of this study are available from the corresponding authors upon reasonable request. Source data are provided with this paper.

Received: 12 July 2021; Accepted: 26 April 2022; Published online: 9 June 2022

References

- Wu, J. & Yang, H. Platinum-based oxygen reduction electrocatalysts. Acc. Chem. Res. 46, 1848–1857 (2013).
- Nørskov, J. K. et al. Origin of the overpotential for oxygen reduction at a fuel-cell cathode. J. Phys. Chem. B 108, 17886–17892 (2004).
- Peng, Z. & Yang, H. Designer platinum nanoparticles: control of shape, composition in alloy, nanostructure and electrocatalytic property. *Nano Today* 4, 143–164 (2009).
- Debe, M. K. Electrocatalyst approaches and challenges for automotive fuel cells. Nature 486, 43–51 (2012).
- Kodama, K., Nagai, T., Kuwaki, A., Jinnouchi, R. & Morimoto, Y. Challenges in applying highly active Pt-based nanostructured catalysts for oxygen reduction reactions to fuel cell vehicles. *Nat. Nanotechnol.* 16, 140–147 (2021).
- Greeley, J. et al. Alloys of platinum and early transition metals as oxygen reduction electrocatalysts. Nat. Chem. 1, 552–556 (2009).
- Rossmeisl, J., Karlberg, G. S., Jaramillo, T. & Nørskov, J. K. Steady state oxygen reduction and cyclic voltammetry. *Faraday Discuss.* 140, 337–346 (2009).
- Zhang, L. et al. Platinum-based nanocages with subnanometer-thick walls and well-defined, controllable facets. Science 349, 412–416 (2015).
- Kitchin, J. R., Nørskov, J. K., Barteau, M. A. & Chen, J. G. Modification of the surface electronic and chemical properties of Pt(111) by subsurface 3d transition metals. *J. Chem. Phys.* 120, 10240–10246 (2004).
- Zhao, Z. et al. Pt-based nanocrystal for electrocatalytic oxygen reduction. Adv. Mater. 31, 1808115 (2019).
- Toda, T., Igarashi, H., Uchida, H. & Watanabe, M. Enhancement of the electroreduction of oxygen on Pt alloys with Fe, Ni, and Co. *J. Electrochem.* Soc. 146, 3750–3756 (1999).
- Stamenkovic, V. R. et al. Trends in electrocatalysis on extended and nanoscale Pt-bimetallic alloy surfaces. Nat. Mater. 6, 241–247 (2007).
- 13. Stephens, I. E. L. et al. Tuning the activity of Pt(111) for oxygen electroreduction by subsurface alloying. *J. Am. Chem. Soc.* **133**, 5485–5491 (2011).
- 14. Escudero-Escribano, M. et al. Tuning the activity of Pt alloy electrocatalysts by means of the lanthanide contraction. *Science* **352**, 73–76 (2016).
- Strasser, P. et al. Lattice-strain control of the activity in dealloyed core-shell fuel cell catalysts. Nat. Chem. 2, 454–460 (2010).
- Kitchin, J. R., Nørskov, J. K., Barteau, M. A. & Chen, J. G. Role of strain and ligand effects in the modification of the electronic and chemical properties of bimetallic surfaces. *Phys. Rev. Lett.* 93, 156801 (2004).
- Liu, Z., Zhao, Z., Peng, B., Duan, X. & Huang, Y. Beyond extended surfaces: understanding the oxygen reduction reaction on nanocatalysts. *J. Am. Chem. Soc.* 142, 17812–17827 (2020).
- Chen, Y., Cheng, T. & Goddard, W. A. III Atomistic explanation of the dramatically improved oxygen reduction reaction of jagged platinum nanowires, 50 times better than Pt. J. Am. Chem. Soc. 142, 8625–8632 (2020).
- 19. Bligaard, T. & Nørskov, J. K. Ligand effects in heterogeneous catalysis and electrochemistry. *Electrochim. Acta* **52**, 5512–5516 (2007).
- Calle-Vallejo, F. et al. Finding optimal surface sites on heterogeneous catalysts by counting nearest neighbors. Science 350, 185–189 (2015).
- Cui, C., Gan, L., Heggen, M., Rudi, S. & Strasser, P. Compositional segregation in shaped Pt alloy nanoparticles and their structural behaviour during electrocatalysis. *Nat. Mater.* 12, 765–771 (2013).
- Cherevko, S., Kulyk, N. & Mayrhofer, K. J. J. Durability of platinum-based fuel cell electrocatalysts: dissolution of bulk and nanoscale platinum. *Nano Energy* 29, 275–298 (2016).
- Calle-Vallejo, F. et al. Why conclusions from platinum model surfaces do not necessarily lead to enhanced nanoparticle catalysts for the oxygen reduction reaction. *Chem. Sci.* 8, 2283–2289 (2017).
- Chattot, R. et al. Surface distortion as a unifying concept and descriptor in oxygen reduction reaction electrocatalysis. Nat. Mater. 17, 827–833 (2018).
- Bu, L. et al. Biaxially strained PtPb/Pt core/shell nanoplate boosts oxygen reduction catalysis. Science 354, 1410–1414 (2016).
- Tian, X. et al. Engineering bunched Pt-Ni alloy nanocages for efficient oxygen reduction in practical fuel cells. Science 366, 850–856 (2019).
- Li, M. et al. Ultrafine jagged platinum nanowires enable ultrahigh mass activity for the oxygen reduction reaction. *Science* 354, 1414–1419 (2016).

- Zhang, C., Hwang, S. Y. & Peng, Z. Size-dependent oxygen reduction property of octahedral Pt–Ni nanoparticle electrocatalysts. *J. Mater. Chem. A* 2, 19778–19787 (2014).
- Wang, C. et al. Correlation between surface chemistry and electrocatalytic properties of monodisperse Pt_xNi_{1-x} nanoparticles. *Adv. Funct. Mater.* 21, 147–152 (2011).
- Huang, X. et al. A rational design of carbon-supported dispersive Pt-based octahedra as efficient oxygen reduction reaction catalysts. *Energy Environ. Sci.* 7, 2957–2962 (2014).
- Fortunelli, A. et al. The atomistic origin of the extraordinary oxygen reduction activity of Pt₃Ni₇ fuel cell catalysts. Chem. Sci. 6, 3915–3925 (2015).
- Gong, M. et al. Optimizing PtFe intermetallics for oxygen reduction reaction: from DFT screening to in situ XAFS characterization. *Nanoscale* 11, 20301–20306 (2019).
- Wang, T. et al. Sub-6 nm fully ordered L1₀-Pt-Ni-Co nanoparticles enhance oxygen reduction via Co doping induced ferromagnetism enhancement and optimized surface strain. Adv. Energy Mater. 9, 1803771 (2019).
- Dutta, I. et al. Electrochemical and structural study of a chemically dealloyed PtCu oxygen reduction catalyst. J. Phys. Chem. C 114, 16309–16320 (2010).
- Hwang, B. J. et al. An investigation of structure—catalytic activity relationship for Pt—Co/C bimetallic nanoparticles toward the oxygenreduction reaction. J. Phys. Chem. C 111, 15267–15276 (2007).
- Moraweck, B., Renouprez, A. J., Hlil, E. K. & Baudoing-Savois, R. Alloying effects on X-ray absorption edges in nickel-platinum single crystals. J. Phys. Chem. 97, 4288–4292 (1993).
- Hlil, E. K., BaudoingSavois, R., Moraweck, B. & Renouprez, A. J. X-ray absorption edges in platinum-based alloys. 2. Influence of ordering and of the nature of the second metal. *J. Phys. Chem.* 100, 3102–3107 (1996).
- Chen, J. et al. Elucidating the many-body effect and anomalous Pt and Ni core level shifts in X-ray photoelectron spectroscopy of Pt–Ni alloys. J. Phys. Chem. C 124, 2313–2318 (2020).
- Mukerjee, S., Srinivasan, S., Soriaga, M. P. & Mcbreen, J. Role of structural and electronic-properties of Pt and Pt alloys on electrocatalysis of oxygen reduction: an in-situ XANES and EXAFS investigation. *J. Electrochem. Soc.* 142, 1409–1422 (1995).
- Rehr, J. J., Kas, J. J., Vila, F. D., Prange, M. P. & Jorissen, K. Parameter-free calculations of X-ray spectra with FEFF9. *Phys. Chem. Chem. Phys.* 12, 5503–5513 (2010).
- Pápai, Z. & Pap, T. L. Analysis of peak asymmetry in chromatography. J. Chromatogr. A 953, 31–38 (2002).
- Kuhn, M. & Sham, T. K. Charge redistribution and electronic behavior in a series of Au-Cu alloys. *Phys. Rev. B* 49, 1647–1661 (1994).
- Jia, Q. et al. Activity descriptor identification for oxygen reduction on platinum-based bimetallic nanoparticles: in situ observation of the linear composition-strain-activity relationship. ACS Nano 9, 387–400 (2015).
- Cao, L. et al. Differential surface elemental distribution leads to significantly enhanced stability of PtNi-based ORR catalysts. *Matter* 1, 1567–1580 (2019).
- Li, J. et al. Hard-magnet L1_o-CoPt nanoparticles advance fuel cell catalysis. *Joule* 3, 124–135 (2019).
- Barcaro, G., Sementa, L. & Fortunelli, A. A grouping approach to homotop global optimization in alloy nanoparticles. *Phys. Chem. Chem. Phys.* 16, 24256–24265 (2014).
- Hu, J. et al. Increasing stability and activity of core–shell catalysts by preferential segregation of oxide on edges and vertexes: oxygen reduction on Ti–Au@Pt/C. J. Am. Chem. Soc. 138, 9294–9300 (2016).
- Jennings, P. C., Aleksandrov, H. A., Neyman, K. M. & Johnston, R. L. A DFT study of oxygen dissociation on platinum based nanoparticles. *Nanoscale* 6, 1153–1165 (2014).
- Arán-Ais, R. M. et al. Elemental anisotropic growth and atomic-scale structure of shape-controlled octahedral Pt-Ni-Co alloy nanocatalysts. *Nano Lett.* 15, 7473-7480 (2015).
- Zhao, Z. et al. Composition tunable ternary Pt-Ni-Co octahedra for optimized oxygen reduction activity. *Chem. Commun.* 52, 11215–11218 (2016).
- Huang, X. et al. High-performance transition metal-doped Pt₃Ni octahedra for oxygen reduction reaction. Science 348, 1230–1234 (2015).
- Huang, J. et al. PtCuNi tetrahedra catalysts with tailored surfaces for efficient alcohol oxidation. *Nano Lett.* 19, 5431–5436 (2019).
- Arruda, T. M., Shyam, B., Ziegelbauer, J. M., Mukerjee, S. & Ramaker, D. E. Investigation into the competitive and site-specific nature of anion adsorption on Pt using in situ X-ray absorption spectroscopy. *J. Phys. Chem. C* 112, 18087–18097 (2008).
- Newville, M. IFEFFIT: interactive XAFS analysis and FEFF fitting. J. Synchrotron Radiat. 8, 322–324 (2001).
- Ravel, B. & Newville, M. ATHENA, ARTEMIS, HEPHAESTUS: data analysis for X-ray absorption spectroscopy using IFEFFIT. J. Synchrotron Radiat. 12, 537–541 (2005).

- Newville, M., Liviņš, P., Yacoby, Y., Rehr, J. J. & Stern, E. A. Near-edge X-ray-absorption fine structure of Pb: a comparison of theory and experiment. *Phys. Rev. B* 47, 14126–14131 (1993).
- Ankudinov, A. L., Ravel, B., Rehr, J. J. & Conradson, S. D. Real-space multiple-scattering calculation and interpretation of X-ray-absorption near-edge structure. *Phys. Rev. B* 58, 7565–7576 (1998).
- Mattheiss, L. F. Energy bands for solid argon. Phys. Rev. 133, A1399–A1403 (1964).
- Giannozzi, P. et al. QUANTUM ESPRESSO: a modular and open-source software project for quantum simulations of materials. *J. Condens. Matter Phys.* 21, 395502 (2009).
- Perdew, J. P., Burke, K. & Ernzerhof, M. Generalized gradient approximation made simple. *Phys. Rev. Lett.* 77, 3865–3868 (1996).
- Vanderbilt, D. Soft self-consistent pseudopotentials in a generalized eigenvalue formalism. *Phys. Rev. B* 41, 7892–7895 (1990).
- Wang, Z., Guo, X., Montoya, J. & Nørskov, J. K. Predicting aqueous stability of solid with computed Pourbaix diagram using SCAN functional. npj Comput. Mater. 6, 160 (2020).
- 63. Chen, C. et al. Highly crystalline multimetallic nanoframes with three-dimensional electrocatalytic surfaces. *Science* **343**, 1339–1343 (2014).
- Gong, M. et al. One-nanometer-thick Pt₃Ni bimetallic alloy nanowires advanced oxygen reduction reaction: integrating multiple advantages into one catalyst. ACS Catal. 9, 4488–4494 (2019).
- Beermann, V. et al. Rh-doped Pt–Ni octahedral nanoparticles: understanding the correlation between elemental distribution, oxygen reduction reaction, and shape stability. Nano Lett. 16, 1719–1725 (2016).
- Lim, J. et al. Ga-doped Pt-Ni octahedral nanoparticles as a highly active and durable electrocatalyst for oxygen reduction reaction. *Nano Lett.* 18, 2450–2458 (2018).
- Bu, L. et al. Surface engineering of hierarchical platinum-cobalt nanowires for efficient electrocatalysis. Nat. Commun. 7, 11850 (2016).

Acknowledgements

Y.H., Q.J., W.A.G. and X.D. gratefully acknowledge the support of the Office of Naval Research (award N000141812155). The XAS data were collected at beamlines 6-BM, 7-BM and 8-ID of the National Synchrotron Light Source II, a US Department of Energy Office of Science User Facility operated for the Department of Energy Office of Science by Brookhaven National Laboratory under contract no. DE-SC0012704. We acknowledge the use of facilities and instrumentation at the University of California Irvine Materials

Research Institute, supported in part by the National Science Foundation Materials Research Science and Engineering Center programme through the University of California Irvine Center for Complex and Active Materials (DMR-2011967). We also thank the Electron Imaging Center of Nanomachines at the California NanoSystems Institute (CNSI) for TEM support. A.F. and W.A.G. received support from the National Science Foundation (CBET-1805022 and CBET-2005250). A.F., G.B. and L.S. gratefully acknowledge the contribution of the International Research Network on Nanoalloys Centre national de la recherche scientifique (CNRS) and computational support from the CINECA supercomputing centre within the Italian SuperComputing Resource Allocation (ISCRA) programme.

Author contributions

J.H., M.F., M.L., Y.L., C.W., S.-J.L., B.P. and Z.L. conducted the synthesis of electrocatalysts, structural characterization and electrochemical experiments. M.X. and J.H. conducted the TEM and EDX characterizations. Q.J., E.L., L.J. and D.L. conducted the XAS studies. A.F., L.S., G.B., Q.J., J.H. and W.A.G. performed the modelling and data analyses. The project was conceived by Y.H. and supervised by Y.H. (project design, syntheses and evaluation of the catalysts); Q.J. (XAS studies); and A.F. and W.A.G. (computational studies). J.H., Y.H., Q.J. and A.F. wrote the original draught. J.H., Y.H., Q.J., A.F., W.A.G. and Z.L. revised the manuscript.

Competing interests

The authors declare no competing interests.

Additional information

Supplementary information The online version contains supplementary material available at https://doi.org/10.1038/s41929-022-00797-0.

Correspondence and requests for materials should be addressed to William A. Goddard, Alessandro Fortunelli, Qingying Jia or Yu Huang.

Peer review information *Nature Catalysis* thanks Janis Timoshenko and the other, anonymous, reviewer(s) for their contribution to the peer review of this work.

Reprints and permissions information is available at www.nature.com/reprints.

Publisher's note Springer Nature remains neutral with regard to jurisdictional claims in published maps and institutional affiliations.

© The Author(s), under exclusive licence to Springer Nature Limited 2022